行政院國家科學委員會專題研究計畫　成果報告

毫米波元組件之適用性分析(3/3)

計畫類別：個別型計畫
計畫編號：NSC91-2219-E-002-028-
執行期間：91 年 08 月 01 日至 92 年 07 月 31 日
執行單位：國立臺灣大學電信工程學研究所

計畫主持人：江簡富
共同主持人：陳俊雄

報告類型：完整報告

處理方式：本計畫可公開查詢

中　華　民　國 92 年 11 月 3 日

Analysis on Bonding Wires

Monsen Leu and Jean-Fu Kiang

Department of Electrical Engineering and
Graduate Institute of Communication Engineering
National Taiwan University
Taipei, Taiwan, ROC
NSC 91-2213-E-002-030

Abstract

Bonding wires are generally used fot high-density I/O interconnection between package and chip die. In this paper, we will analyze bonding wires using an electrostatic approach, discuss their electrical characteristics, and propose some improvement methods Different configurations of bonding wire array are compared, and guidelines for designing will also be proposed.

1 Introduction

Bonding wires are used to connect chip die to pads of a package, which have low cost, high reliability, high manufacturability and high I/O wire density[2]. Wire bonding parameters include wire pitch, loop height, wire profile, wire material and encapsulation materials defined in the standard of JEDEC-JESD59 [3]. All the bonding wires in a package are encapsulated in a molded compound which is usually an epoxy with $\epsilon_r = 4.2$ [3]. The wires are usually made of gold ($\sigma = 4.1 \times 10^7$S/m) and has a diameter of 1-2 mils, length of 0.5-4.5 mm, wire pitch of greater than 80 μm [4]. Electrical performance of a bonding wire is limited by its parasitic inductance [3]. The inductance of a bonding wire is determined by the magnetic field distribution induced by the current on the bonding wire and its return path. The loop includes the bonding wire, ground plane, ground via to the ground ring, and a bonding wire from the ground ring pad to the die pad. In generally, self and mutual inductances are larger for larger loops.

2 Modeling Technigue

To analyze high frequency effects, wire geometry, operating frequency, dielectric constant, loss tangent, conductivity, permittivity, and so on have to be considered. As the chip size is reduced, measurements become more difficult because there are so many parasitic effects which may affect the signal-to-noise ratio(S/N). To overcome the measurement difficulties, one may use EM simulation and build equivalent circuit to predict the high frequency effects.

When the length of bonding wire is shorter than $\lambda/100$, lumped element model can be used. The wire loop can be modeled as an inductor with the self and mutual inductance calculated by using quasi static approach. For more accurate prediction of bonding wire, pad capacitance and resistance can be incorporated to form a π-model. To adjust the model to account for manufacturing tolerrance, fine tune to fit measurement method can be adopted [1].

3 Inductance

Fig.1 shows a bonding wire above ground plane, which is equivalent to a closed current loop by using image theory.

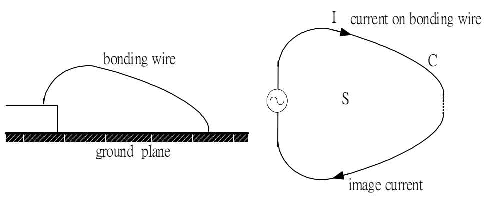

Figure 1: The image of bonding wire

Inductance of a wire loop carrying current I is defined as:

$$L = \frac{1}{I}\frac{\mu}{4\pi}\oint_C \oint_C \frac{I(\bar{r}')}{|\bar{r}-\bar{r}'|} d\bar{\ell}' \cdot d\bar{\ell}$$

The current loop can be divided into M segments and the inductance can be decomposed into M^2 partial inductance as

$$L = \sum_{p=1}^{M}\sum_{q=1}^{M} \frac{\mu}{4\pi}\oint_{C_p}\int_{C_q} \frac{1}{|\bar{r}-\bar{r}'|} d\bar{\ell}' \cdot d\bar{\ell}$$

where L_{pq} is the partial inductance on segment p contributed by the current on segment q.

Inductance of a bonding wire loop is determined by the total magnetic flux linkages contributed by self and nearby bonding wire loops. The induced voltage at loop m is

$$V_m = \frac{d\psi_m}{dt} = \frac{d}{dt}\sum_{N=1}^{w} L_{mn} I_n$$

where ψ_m is the total magnetic flux through loop m, L_{mn} is the mutual inductance from loop n to loop m.

$$L_{mn} = \frac{\mu}{4\pi}\oint_{C_m}\oint_{C_n} \frac{d\bar{\ell}'_n \cdot d\bar{\ell}_m}{|\bar{r}-\bar{r}'|}$$

Each bonding wire loop can be approached by a polygon combination. The L_{mn} can be calculation as the summation of partial inductance L_{mn}^{pq} which is from the q line segment at $\bar{r}'$ of loop m to the p line segment at $\bar{r}$ of loop n.

$$L_{mn} = \sum_{p=1}^{M_m}\sum_{q=1}^{M_n} \frac{\mu}{4\pi}\int_{C_{mp}}\int_{C_{nq}} \frac{d\bar{\ell} \cdot d\bar{\ell}'}{|\bar{r}-\bar{r}'|} = \sum_{p=1}^{M_m}\sum_{q=1}^{M_n} L_{mn}^{pq}$$

In calculating L_{mn}^{pq}, the q line segment at $\bar{r}'$ of loop m is rotated to +Z axis with a segment length h from the original point by coordinate rotation and the p line segment at $\bar{r}$ of loop n is rotated to the XZ plane.

4 Capacitance

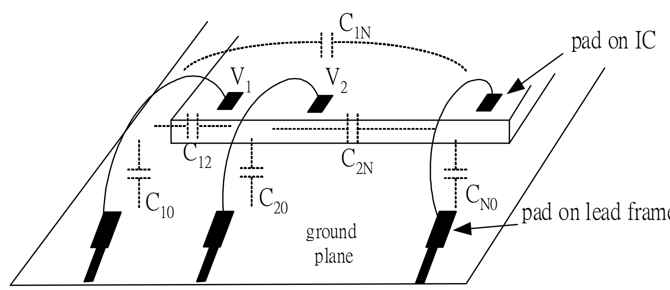

Figure 2: The capacitance of Bonding wires

Fig.2 shows the capacitances of bonding wires above ground plane. Charges on bonding wires are related to pad voltages on IC as

$$Q_1 = (C_{10}\cdots + C_{1N})\,V_1 \cdots - C_{1N}V_N$$

$$\vdots$$
$$Q_N = -C_{1N}V_1 \cdots + (C_{1N} \cdots + C_{No})\, V_N$$

Compared with the matrix form,

$$\begin{bmatrix} Q_1 \\ Q_2 \\ \vdots \\ Q_N \end{bmatrix} = \begin{bmatrix} c_{11} & c_{12} & \cdots & c_{1N} \\ c_{21} & c_{22} & & c_{2N} \\ \vdots & & \ddots & \\ c_{N1} & c_{N2} & & c_{NN} \end{bmatrix} \begin{bmatrix} V_1 \\ V_2 \\ \vdots \\ V_N \end{bmatrix}$$

the capacitance can be expressed as

$$C_{in} = -c_{in} \qquad \text{for n = 1,....,N and n} \neq \text{i}$$
$$C_{i0} = \sum_{n=1, n\neq i}^{N} c_{in}$$

, where i is the bonding wire number, C_{in} is a mutual capacitance between wire i and wire n, and C_{i0} is the capacitance to ground. By using electrostatic electric calculation, the voltage of a bonding wire above ground plane can be expressed as

$$V(\bar{r}) = \int_C \frac{\rho(\bar{r}')}{4\pi\varepsilon} \left(\frac{1}{|\bar{r} - \bar{r}'|} - \frac{1}{|\bar{r} - \bar{r}'_I|} \right) d\ell'$$

where $|\bar{r} - \bar{r}'|$ is the distance bewteen charge and obvservation point on wire surface, $|\bar{r} - \bar{r}'_I|$ is the distance bewteen the image charge and the observation point , and $\rho(\bar{r}')$ is line charge density.

Similar to inductance calculation, the nth bonding wire is partitioned into M_n segments. The voltage V_m^p on segment p of mth bonding wire is

$$V_m^p(\bar{r}) = \sum_{n=1}^{N} \sum_{q=1}^{M_n} \frac{\rho_n^q}{4\pi\varepsilon} \int_{C_n^q} \left(\frac{1}{|\bar{r} - \bar{r}'|} - \frac{1}{|\bar{r} - \bar{r}'_I|} \right) d\ell'$$

where the line charge density at segment q is assumed to be a constant ρ_n^q. Intergrating V_m^p over segment p and assuming V_m^p to be constant, the equations becomes

$$V_m^p = \sum_{n=1}^{N} \sum_{q=1}^{M_n} \frac{\rho_n^q}{4\pi\varepsilon\ell_m^p} \int_{C_m^p} d\ell \int_{C_n^q} d\ell'$$
$$\left(\frac{1}{|\bar{r} - \bar{r}'|} - \frac{1}{|\bar{r} - \bar{r}'_I|} \right)$$

which can be calculated as the inductance calculation.

5 Resistance

DC resistance of a long wire line with radius a and conductivity σ is

$$R_{dc} = \ell \times \frac{1}{\sigma\pi a^2} \tag{1}$$

The rf resistance of a long wire line with radius a, conductivity σ at frequency f is

$$R_{rf} \cong \ell \times \frac{1}{\sigma 2\pi a\delta} \tag{2}$$
$$= \ell \times \frac{1}{2a}\sqrt{\frac{\mu}{\pi\sigma}}\sqrt{f} \tag{3}$$

6 Comparisons with Canonical cases

Here are tables which shows the inductance of the close forms and the quasi-static polylines calculation. The self inductance of a equilateral triangle loop is [6]

$$Ls \cong \frac{3\mu s}{2\pi}\left(\log\left|\frac{s}{r}\right| - 1.40546\right)$$

The self inductance of a circular loop is [5]

$$Ls \cong \mu R \left(\log\left|\frac{8R}{a}\right| - 2\right)$$

The cirular loop is segmented into 16 parts and 32 parts to compare with the close form formula.

The mutual inductance between two circular loops is [7]

$$M \cong \mu\sqrt{a1a2}\frac{2}{k}\left(\left(1 - \frac{k^2}{2}\right)K(k) - E(k)\right)$$

Table 1: Self inductance of a equilateral triangle loop[6].

$r(\mu\text{m})$	$s(\mu\text{m})$	$[6](nH)$	This work(nH)
12.7	250	0.23616	0.26145
12.7	500	0.68026	0.70963
12.7	1000	1.77642	1.81004
25.4	500	0.47232	0.51008
25.4	1000	1.36053	1.40402

Table 2: Self inductance of a circular loop[5].

r	R	[5]	16	32
12.7	100	0.26930	0.26742	0.28583
12.7	500	2.35733	2.31466	2.35236
12.7	1000	5.58650	5.49475	5.56316
12.7	2500	16.84490	16.60486	16.77663
12.7	5000	38.04490	37.54757	37.90518

$$, k = \sqrt{\frac{4a1a2}{(a1+a2)^2 + h^2}}$$

Table 3: Mutual inductance between two circular loops[7].

$a1$	$a2$	h	[7]	32 segment
500	500	5	2.94350	2.93258
500	500	50	1.50144	1.49454
500	500	500	0.24704	0.24509
500	2500	50	0.20030	0.19966

7 Comparison with Hai-Young Lee

In Hai-Young Lee's research, the bonding wire are parallel or with internal angle of 30 degrees.

In Hai-Young Lee's research on bonding wire of length 500μ m, the inductance by quasi-static calculation is almost the same as

Table 4: Inductance of bonding wirers[8][9][10].

L	length (μm)	$s(\mu\text{m})$	MOM	This work(nH)
L_s	500		0.278	0.27831
L_m	500	20	0.250	0.22565
L_m	500	50	0.128	0.13011
L_m	500	100	0.071	0.69294
L_m	500	200	0.028	0.02686
L_m	500	30	0.085	0.08551

the inductance by monent method below 30 GHz as[8][9][10]

$$\left|\frac{L(30G) - L(0)}{L(0)}\right| \times 100\% = 3.06\%$$
$$\left|\frac{M(30G) - M(0)}{M(0)}\right| \times 100\% = 8.06\% \qquad (4)$$

In [11], BGA can operate up to 31GHz, at which the quasi-static calculation for bonding wires is sufficient.

8 Conclusion

By comparing with the close form formula and MOM method, the qusai-static method is accurate and fast calculation. The method can be used up to 30 Ghz with acceptable errors. Any shapes of bonging wire can be calculated, and only some sampleing points is needed with the polygons is approximate the real shape.

References

[1] S. Pinel, S. Chakraborty, M. Roellig, R. Kunze, S. Mandal, H. Liang, C.-H. Lee, R. Li, K. Lim, G. White, M. Tentzeris, and J. Laskar, "3D integrated LTCC module using muBGA technology

for compact C-band RF front-end module," *IEEE MTT-S Int. Microwave Symp. Dig.*, vol.3, pp.1553-1556, 2002.

[2] A. Sutono, N.G. Cafaro, J. Laskar, and E. Tentzeris,"Experimental study and modeling of microwave bond wire interconnects," *IEEE AP-S. Int. Symp. Dig.,* Salt Lake City, UT, pp.2020-2023, 2000.

[3] A. C. W. Lu, F. Wei, L.L. Wai, L.A. Low, F.X. Ke, K.C. Yip, and Y.P. Lim,"Modeling and characterization of wire bonding for RF applications," *IEEE Electron. Comp. Technol. Conf.*, pp.905 -909, 2002.

[4] R. R. Tummala, E.J. Rymaszewski, A.G. Klofenstein, *Microelectronics Packageing Handbook*, New York: Van Nostrand Reinhold, 1989.

[5] C. S. Walker, *Capacitance, Inductance and Crosstalk analysis*, Artech House, 1990.

[6] F. W. Grover, *Inductance Calculations: Working Formula and Tables*, Dover Publications, Inc., New York, 1946

[7] C. Akyel, S. babic, S. Kincic,"New and fast procedures for calculating the mutual inductance of coaxial circular coils(circular coil-disk coil)," *IEEE Trans. Magn.,* vol.38, no.5, pp. 2367-2369, sept. 2002.

[8] H. Y. Lee,"Wideband characterization of mutual coupling between high density bonding wires," *IEEE Microwave Guided Wave Lett.,* vol.4, no.8, pp. 265-267, Aug. 1994.

[9] H. Y. Lee,"Wideband characterization of a typical bonding wire for microwave and millimeter-wave integrated circuits," *IEEE Trans. Microwave Theory Tech.,* vol.43, no.1, pp. 63-68, Jan. 1995.

[10] S. K. Yun and H. Y. Lee, "Parasitics impedance analysis of double bonding wires for high-frequency integrated circuit packageing," *IEEE Microwave Guided Wave Lett.,* vol.5, no. 9, pp. 296-298, Sep. 1995.

[11] M. P. R. Panicker, D. Douriet, M. S. Hyslop, and N. L. Greenman,"Ball grid arrays: A DC to 31.5GHz low cost packaging solution for microwave and mm-wave MMICs," *Microwave J.,* pp.158-168, Jan. 1998.

Dielectric Resonator Antenna with Slit

Tsung-Shan Yang and Jean-Fu Kiang
Department of Electrical Engineering and
Graduate Institute of Communication Engineering
National Taiwan University

NSC 91-2213-E-002-030

Abstract

This paper presents a rectangular DR antenna with slit, fed by a coaxial probe. Slit at different positions in the DR modify the input impedance and resonant frequency of the TE^z_{111} and the TE^z_{211} modes to different extent. The DR antenna with a slit has a broad bandwidth and lower Q factor compared with without slit.

1 Introduction

Since the introduction of dielectric resonator antenna (DRA) in 1983 [1], there is a growing interest to improve their radiation characteristics [2]-[7]. In [2], [3] and [7], multiple coupled resonators are used to broaden the bandwidth or to achieve dual band. In [4], an air gap between conductor and dielectric due to fabrication tolerance broadens the bandwidth and reduces the Q factor of the DR antenna. In this paper, a rectangular DR antenna with a slit is proposed to enhance its performance.

2 Rectangular DR with Center Slit

Consider a rectangular DR antenna, in which the feed probe is attache to the side wall of DR to excite the TE^z_{111} mode as shown in Fig.1. A narrow slit is drilled in the middle of the rectangular DR antenna, where the strongest electric field of TE^z_{111} mode appears normal to the slit wall. Contrast of dielectric constant between slit and dielectric further enhance the electric field in the slit.

Fig.2 shows the return loss associated with TE^z_{111} mode of a rectangular DR antenna with different slit width. Notice that the coaxcial probe length, h, controls the coupling between DR and coaxcial probe. In order to obtain a good impedance match for these structures, the probe length with solid DR antenna is 8.5 mm, and the probe length with the DR antenna with slit is 12.5 mm. As shown in Fig.2, the 10 dB bandwidth is 6.4 % with a slit of 4 mm width, higher than the bandwidth of 2.1 % without slit. The resonant frequency is also increased with increasing slit width due to the pertubation of slit.

Fig.3 shows the radiation pattern of the antenna in Fig.1. The pattern is similar to that of the DR antenna without slit. Since the ground plane is finite, the back radiation still exists.

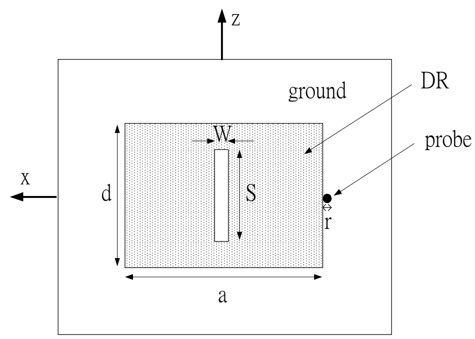

(a)

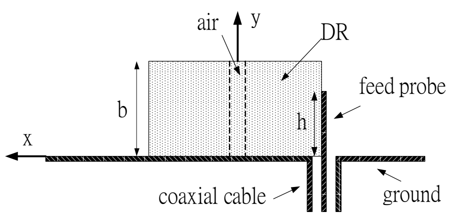

(b)

Figure 1: Rectangular DRA with center slit, (a) top view, (b) side view.

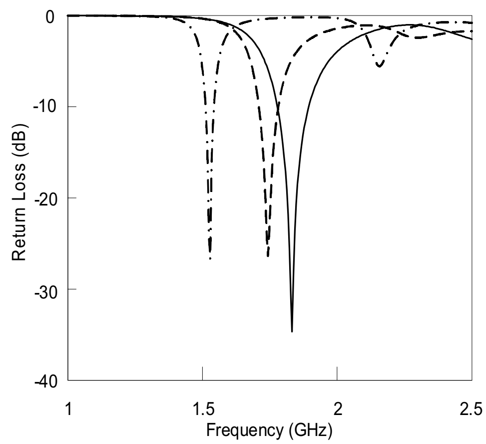

Figure 2: Return loss versus frequency for the rectangular DR antenna with different center slit widths, $\epsilon_r = 40$, $a = 26.5$ mm, $b = 13$ mm, $d = 19.4$ mm, $r = 1$ mm, $S = 13.4$ mm, ground size is 50 mm $\times$ 40 mm, $- \cdot -$: no slit, - - -: W=2 mm, —: W=4 mm.

3 Rectangular DR with Side Slit

Next, study the effects of an air gap drilled near one side of the rectangular DR as shown in Fig.4. The slit is placed asymmetrically with respect to the center axis where the strongest electric field associated with TE^z_{211} mode is normal to the slit wall. Hence, the side slit is expected to cause stronger effect on the TE^z_{211} mode than on the TE^z_{111} mode.

Fig.5 shows the return loss of a rectangular DR antenna with different side slit widths. In our simulation, the rectangular DR antenna without side slit can not obtain good impedance match concurrently for both the TE^z_{211} and TE^z_{211} modes. The return loss of the DR antenna without slit for the TE^z_{111} mode is well matched but the TE^z_{211} mode is not, as shown in Fig.5. However, with proper choice of side slit in the DR antenna, the return loss below 10 dB for both modes can be obtained concurrently.

The far-field patterns associated with the TE^z_{211} mode of the DR antenna with side slit are shown in Fig.6. With side slit, the null in $\hat{y}$ direction for the TE^z_{211} mode vanishes. Because the side slit breaks the symmetry between two circular type electric field distributions in an otherwise solid DR.

4 Conclusions

The effects of a slit in rectangular DR antennas have been studied in this paper. The TE^z_{111} and TE^z_{211} modes are excited. Discontinuity of normal electric field at the interface between

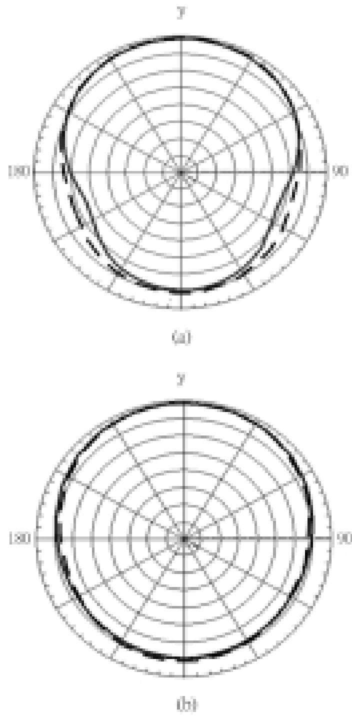

Figure 3: Far-field patterns for the antenna in Fig.1, (a) E_ϕ on the x-y plane, (b) E_ϕ on the y-z plane, - -: no slit, —: W=4 mm.

air and dielectric incurs a stronger electric field in the slit. The center slit in a DR antenna has stronger effect on the TE^z_{111} mode and a side slit has stronger effect on the TE^z_{211} mode. The slits broaden the bandwidth, lower the Q factor, and increase the resonant frequency of both the TE^z_{111} and TE^z_{211} modes.

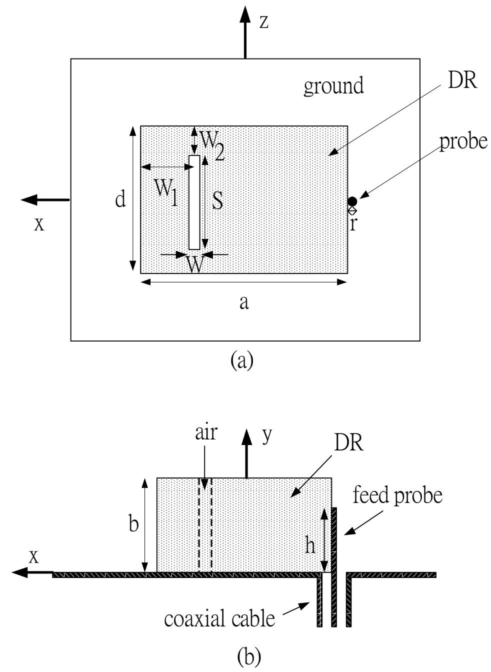

Figure 4: Rectangular DR antenna with a side slit, (a) top view, (b) side view.

References

[1] S. A. Long, M. W. McAllister , and L. C. Shen, "The resonant cylindrical dielectric cavity antenna," *IEEE Trans. Antennas Propagat.,* vol. 31, pp. 406-412, May 1983.

[2] A. A. kishk, B. Ahn, and D. Kaifez, "Broadband stacked dielectric resonator antennas," *Electron. Lett.,* vol.25, no.18, pp.1232-1233, Aug. 1989.

[3] S. M. Shum and K. M. Luk, "Stacked annular ring dielectric resonator antenna excited by axi-symmetric coaxial probe," *IEEE Trans. Antennas Propagat.,* vol. 43, no. 8, pp. 889-892, Aug. 1995.

[4] G. P. Junker, A. A. Kishk, A. W. Glisson, and D. Kajfez, "Effect of fabrication imperfections for ground-plane-backed dielectric-resonator antennas," *IEEE Antennas Propagat. Mag.,* vol. 37, no.1, pp. 40-47, Feb. 1995.

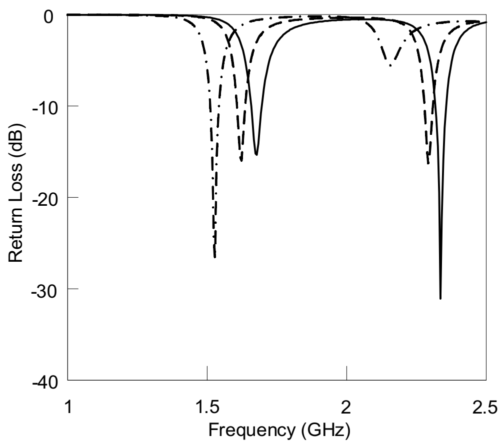

Figure 5: Return loss of rectangular DR antenna with different side slit widths, $\epsilon_r = 40$, $a = 26.5$ mm,$b = 13$ mm, $d = 19.4$ mm, $h = 8.5$ mm, $r = 1$ mm, $W_1 = 5.75$ mm, $W_2 = 3$ mm, $S = 13.4$ mm, ground size is 50 mm $\times$ 40 mm, $- \cdot -$: no slit, - - -: W=2 mm, —: W=4 mm.

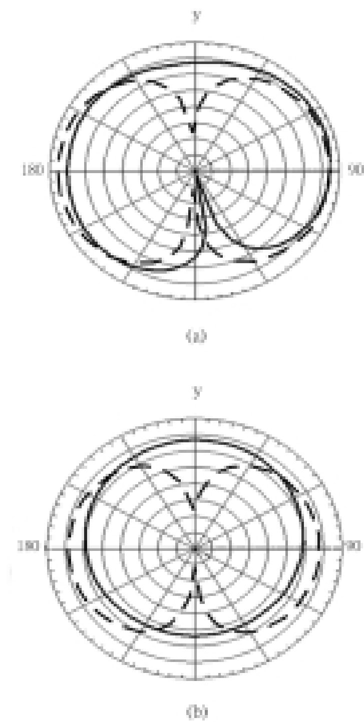

Figure 6: Far-field patterns associated with the TE^z_{211} mode for the antenna in Fig. 4, (a) E_ϕ on the x-y plane, (b) E_ϕ on the y-z plane, - -: no slit, —: W=4 mm.

[5] K. W. Leung, "Complex resonance and radiation of hemispherical dielectric-resonator antenna with a concentric conductor," *Trans. Microwave Theory Tech.,* vol.49, no.3, pp.524-531, Mar. 2001.

[6] A. Sangiovanni, J. Y. Dauvignac, and C. Pichot, "Embedded dielectric resonator antenna for bandwidth enhancement," *Electron. Lett.,* vol. 33, no. 25, pp. 2090-2091, Dec. 1997.

[7] Z. Fan and Y. M. M. Antar, "Slot-coupled DR antenna for Dual-frequency operation," *IEEE Trans. Antenna Propagat.,* vol. 45, no. 2, pp. 306-308, Feb. 1997.

[8] R. K. Mongia and P. Bhartia, "Dielectric resonator antennas-A review and general design relations for resonant frequency and bandwidth," *Int. J. Microwave Millimeter Wave Comput.-Aided Eng.,* vol.4, no.3, pp.230-247, 1994.

[9] R. K. Mongia, " Theoretical and experimental investigations on rectangular dielectric resonators," *IEE Proc. H,* vol.139, no.1 pp.98-104, Feb. 1992.

[10] R. K. Mongia and A. Ittipiboon, "Theoretical and experimental investigations on rectangular dielectric resonator antennas," *IEEE Trans. Antennas Propagat.,* vol. 45, no. 9, pp. 1348-1356, Set. 1997.

Design of Multilayered Ring Filters

Chih-Feng Chou and Jean-Fu Kiang

Department of Electrical Engineering and
Graduate Institute of Communication Engineering
National Taiwan University
No.1, Sec.4, Roosevelt Rd.
Taipei, Taiwan 106, ROC
E-mail: jfkiang@cc.ee.ntu.edu.tw
NSC 91-2213-E-002-030

Abstract–A novel microsrtip multilayered ring filter has been proposed. The filter uses multilayered topology to reduce circuit area by cascading resonators in layers. This work also provides a method to control the transmission zero by using equivalent circuit analysis.

Keywords – multilayered ring filter, equivalent circuit, transmission zero

Ⅰ. INTRODUCTION

Conventional approach used to design filters include Butterworth (maximally flat), Chebyshev (equal ripple), and elliptic [1]. The maximally flat design has a flat response in the pass-band, but the slope of band edge is smaller than other designs. The slope of band edge of the equal-ripple design is greater than that of the maximally flat design by about $2^{2N}/4$ where N is the order of filter, but it has ripples of equal amplitude in the pass-band. Elliptic design is a variation of equal-ripple design with even better stop-band characteristics. These three approaches can be implemented in lumped element and some simple resonators.

Recently, microstrip resonators have been widely used in planar filter including ring, half-wavelength lines. They can provide sharper stop band slope. Although they can provide sharper performance, they need the area about $\lambda/2$ x $\lambda/2$ or $\lambda/4$ x $\lambda/4$. If we want the sharper the stop band slope, we always use cascading topology. This will make the big area about n x $\lambda/2$ x $\lambda/2$ or n x $\lambda/4$ x $\lambda/4$. This is not the result we want.

In our communication system especially wireless communication system, the requirement of the area is very important. We all want to save the system total area to let everyone convenient. Recently, it has a new topology been proposed. That is multilayer topology. In our RF front-end wireless system, passive component area always bigger than active component about hundred times. If we can save the passive component area, it means we can save the whole system area by the same proportion. This is very attractive. In this work, we will present the multilayer ring filter using multilayer topology to save the area.

Ⅱ. RING FILTER

Ring filter as shown in Fig.1 can be seen as the variable from the half-wavelength filter as shown in Fig. 2. The half-wavelength resonator is used the open half-wavelength transmission line‘s characteristic and

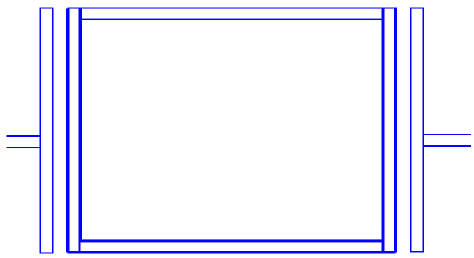

Fig. 1 The schematic of ring filter

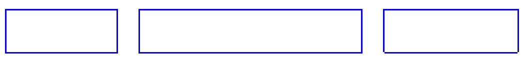

Fig. 2 The schematic of half-wavelength filter

the ring filter can be seen as two open half-wavelength. Basically, the ring filter will get better performance than conventional half-wavelength filter.

Conventional ring filter has line-to-ring coupling structure [2]. Its ring circle length is about the times of our center frequency. In [2], the microstrip line coupled to a circular ring via an air gap, but the insertion loss is high. In order to reduce the insertion loss, coupling structures can be changed from conventional gap capacitor to interdigited capacitor. This will make the bigger capacitance and reduce the coupled loss between the feed line and ring resonator.

There is a different kind of ring filter. It doesn't use the line-to-ring coupling structure. It is direct-connected ring structure [3] with tuning stubs to control the resonant frequency. It doesn't use the gap capacitor structure, so its insertion loss is lower than the line-to-ring coupling.

We can analysis the two kinds of ring filter using the equivalent circuit method. Equivalent circuits of the structure are shown in [3] [4]. From the equivalent circuit, we can get the characteristics of the ring easily.

The line-to-ring coupled structure is a band-pass filter (BPF), capacitance of the coupled structure can be controlled to form narrow band BPF. The direct-connected structure utilizes band-stop characteristics of two stop-bands to construct a wide pass-band. In general, the line-to-ring coupling structure is suitable to build narrow band BPF, and the direct-connected structure is suitable to build broadband BPF.

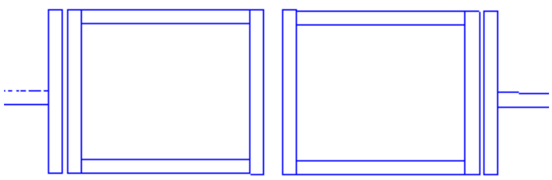

Fig. 3 Cascaded square rings.

Sharper response can be obtained by cascading several resonators as shown in Fig. 3[4]. However, the circuit size will be increased proportional to the number of resonators. A multilayered ring structure is proposed to reduce circuit size.

III. DESIGN of MULTILAYERED RING FILTER

There are many kinds of resonator filters. The most typical one is half-wavelength resonator filter as shown [4]. Because it needs the half-wavelength line, it has very big size and its stop band curve slope is not sharp enough. This is not our hope.

After this configuration, the ring filter has been proposed. A ring structure can be equivalent to two half-wavelength lines. According to the structure, the size will no longer so long. It gets shorter. In another way, due to the more resonators, it get sharper stop band slope. The structure as shown in [4] will become the structure as shown in Fig. 3 and it will get better performance.

According to the two ring resonator structure, it has too big area. In order to solve the problem, we propose the multilayered ring structure. This structure preserves the features of two coupled rings and saves the area by about 50%. The equivalent circuit of the multilayered ring filter is shown in Fig. 4.

IV. EQUIVALENT CIRCUIT of MULTILAYERED

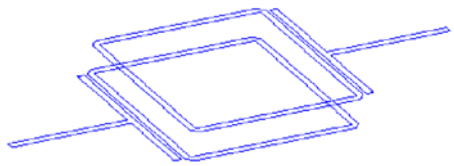

Fig. 4 The schematic of multilayered ring filter

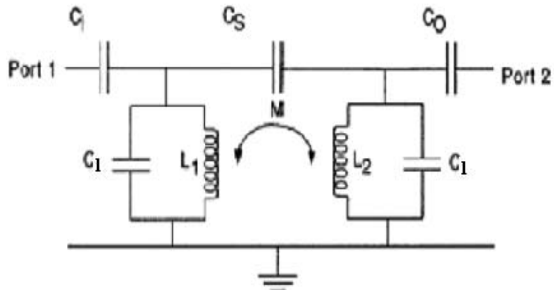

Fig. 5 The equivalent circuit of multilayered ring filter

Here we will analysis the multilayered ring filter with the equivalent circuit. The equivalent circuit as mentioned above used the transmission line model. In this work, we will use the basic lumped element to combine the equivalent circuit as shown in Fig. 5.

From the equivalent circuit, we can easily find that this structure is a band-pass filter. It has two parallel resonators. In order to simplify the equivalent circuit, we use the symmetry structure. That's $C_I = C_O = C_0$ and $L_1 = L_2$. We can analysis this circuit into three parts. One is the front part consisted with $C_I = C_0$. Another part is the center part consisted with the two resonators, coupling capacitor and mutual inductance. The other part is the end part consisted with $C_O = C_0$. We use the ABCD matrix to combine these three parts as shown in Equation (1).

$$\begin{bmatrix} A & B \\ C & D \end{bmatrix} = \begin{bmatrix} A_1 & B_1 \\ C_1 & D_1 \end{bmatrix} \begin{bmatrix} A_2 & B_2 \\ C_2 & D_2 \end{bmatrix} \begin{bmatrix} A_3 & B_3 \\ C_3 & D_3 \end{bmatrix} \quad (1)$$

where

$$\begin{bmatrix} A_1 & B_1 \\ C_1 & D_1 \end{bmatrix} = \begin{bmatrix} A_3 & B_3 \\ C_3 & D_3 \end{bmatrix} = \begin{bmatrix} 1 & \dfrac{1}{j\omega C_0} \\ 0 & 1 \end{bmatrix}$$

$$\begin{bmatrix} A_2 & B_2 \\ C_2 & D_2 \end{bmatrix} = \begin{bmatrix} \dfrac{L_1+\omega^2(C_1+C_s)(M^2-L_1^2)}{M+\omega^2 C_s(M^2-L_1^2)} & \dfrac{1}{j\omega C_s} \\ \dfrac{1-\omega^2 C_1(M-L_1)}{j\omega(M+L_1)} * \dfrac{M+L_1+\omega^2 C_s(M^2-L_1^2)}{M+\omega^2 C_s(M^2-L_1^2)} & 1+\dfrac{C_1}{C_s}-\dfrac{1}{\omega^2 C_s L_1} \end{bmatrix}$$

Then we can use the ABCD matrix to get the S-parameter matrix. Thus, we can know the characteristic of the multilayered ring filter. From the S_{21} of the center part of the equivalent circuit, we can find that there is a transmission zero in our structure as shown in Equation (2)

$$\omega_z = \omega_0 \sqrt{\frac{k_M}{k_E(1-k_M^2)}} \qquad (2)$$

where

$$k_M = \frac{M}{L_1}$$

$$k_E = \frac{C_s}{C_1}$$

$$\omega_0 = \frac{1}{\sqrt{L_1 C_1}}$$

We can control our transmission zero frequency by changing the mutual inductance and mutual capacitance between two coupled rings. This will make our stop band rejection better.

V. SIMULATION RESULTS

In this work, we design a multilayered ring filter. This design is just for making sure if there is a transmission zero or not. The simulation result is shown in Fig. 6.

We can find there is a transmission zero in the upper stop band. This is shown that our theory is correct. During this work, we get a multilayered filter which insertion loss is about 0.8dB and return loss is about 12dB between 2.6 GHz and 2.75GHz.

In this work, stop band curve slope is about 40dB /GHz. Comparing with another structure – multilayered half-ring filter as shown in Fig.7, it has

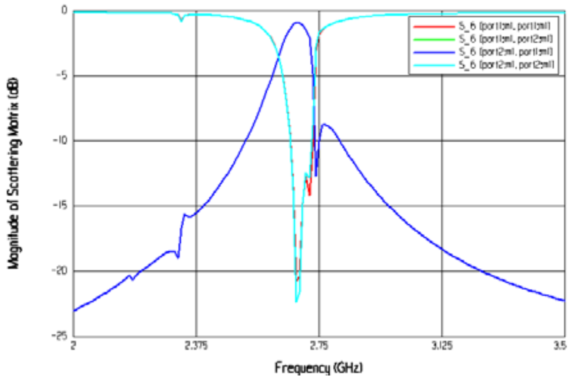

Fig. 6 The simulation result of multilayered ring filter

sharper stop band slope. The multilayered half-ring filter's stop band curve slope is about 30dB /GHz as shown in Fig. 8.

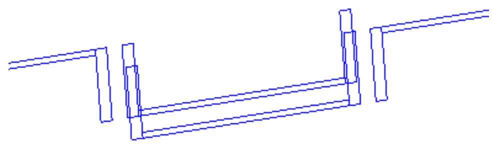

Fig. 7 The schematic of multilayered half-ring filter

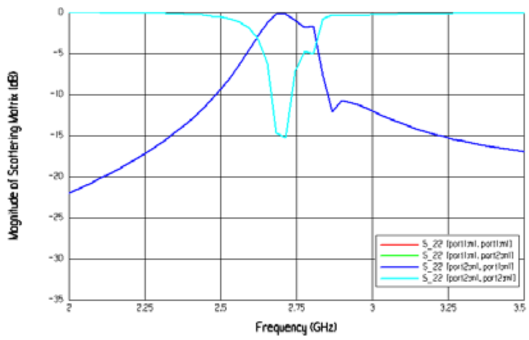

Fig. 8 The simulation result of multilayered half-ring filter

We can find that the multilayered ring filter's performance is better than multilayered half-ring filter. This is because the ring filter has more resonators than half-ring filter. Following this rule, if we want get sharper stop band slope, we don't need more planar area as the planar structure does. We just use more layers as shown in Fig. 9. It doesn't make our area bigger. This is the best advantages of multilayered ring filter.

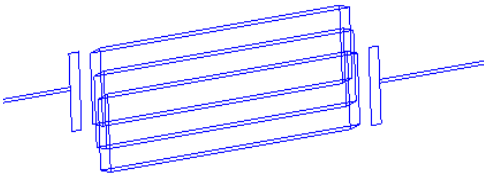

Fig. 9 The simulation result of three layer multilayered ring filter

Ⅵ. CONCLUSION

A novel type of microwave ring filter structure by using multilayer topology has been proposed. By changing the mutual capacitance and mutual inductance, the transmission zero frequency can be controlled. The multilayered ring filter can be improved by making more layers easily and doesn’t need more area to contain the structure. For example, the two layers ring filter’s area is the same with the three layers or four layers ring filter. This is the excellent advantage of multilayered ring filter.

REFERENCES

[1] D. M. Pozar, " *Microwave Engineering*, " 2nd. New York :Wiley, 1998

[2] L. Zhu and K. Wu, "A joint field/circuit model of line-to-ring coupling structures and its application to the design of microstrip dual-mode filters and ring resonator circuits," *IEEE Trans. Microwave Theory Tech.* , vol.47, no.10, pp.1938-1948, Oct. 1999.

[3] L. Hsieh and K. Chang, "Compact, low Insertion-Loss, sharp-rejection, and wide-band microstrip bandpass filters, " *IEEE Trans. Microwave Theory Tech.*, vol.51, no.4, pp.1241-1246, April. 2003.

[4] C. Yu, and K. Chang, "Novel compact elliptic-function narrow-band bandpass filters using microstrip open-loop resonators with coupled and crossing lines," *IEEE Trans. Microwave Theory Tech.*, vol.46, no.7, pp.952-958, July. 1998.

[5] K. Chang, “Microwave Ring Circuits and Antennas.” New York: Wiley, 1996

Input Impedance of Mesh Antenna

Tze-Hsuan Chang and Jean-Fu Kiang

Department of Electrical Engineering and
Graduate Institute of Communication Engineering
National Taiwan University
Taipei, Taiwan, ROC
NSC 91-2213-E-002-030

Abstract

In this paper, we present a simple and general equivalent circuit to model the mesh antenna, investigate several antenna parameters such as input impedance and resonant frequency. The current flow of the mesh is different from patch antenna and disturb the radiation pattern of original patch.

1 Introduction

In [1], a mesh antenna excited with a balanced feed (MA-B) reveal a linearly polarized wave without cross-polarization component in the principal planes. mesh antanna with an unbalanced (MA-U) feed excitation creates almost the same radiation characteristics as balanced feed. A mesh antenna with perturbation elements excited by unbalance feed(MA-UP) generates circular polarization. Loop antennas printed on dielectric substrate can radiate both linearly and circular polarization. MA-U can act as a dual linearly polarization radiation element by selecting the feed point. The cross-meshed array antenna has four feed point a, b, c and d. Changing the feed current phase can radiate linearly or circular polarization [2].

Mesh antennas have wider bandwidth but lower gain than their solid components. In [3], a circular grid patch antenna with the grid lines along the direction of currents flowing on the original patch can be used to excite wanted (exciting) mode and suppress unwanted mode. Modifying mesh geometry for a given mode may increase the cross polarization. Increasing grid density raise the resonant frequency. Meshing the patch improve the gain and decrease the cross polariztion. The gain varies with mesh grometry and density, and are lower than that of standard patch antenna. However, this is achieved at the expense of the front-to-back radiation levels.

In [4], the dichroic microstrip antenna concept is based on the utilization of printed frequency selective mesh as microstrip patch antennas at frequency f_L, which in turn become transparent to near-field radiation at f_H from another microstrip array in close proximity. This technique can separate f_L and f_H many octaves. The use of higher permittivity substrates may lead to some bandwidth restrictions and some increased mesh dissipation loss.

In [5], the operation of linear wire-grid array is argued that the current phasing be adjuested such that radiation by currents on long segments cancel while that by currents on short segments combine constructively. The short segments are considered as discrete elements fed via microstrip transmission lines that these antennas are viewed as arrays.

The resonant frequency is defined as the frequency where the return loss is maximum. Measurement result shows that the resonant frequency decreases with increasing mesh spacing when the same dimension of radiating elements [6]. The bandwidth is defined by the criterion that the VSWR is less than 2. Bandwidth increases with increasing mesh spacing. Higher gain can be obtained by using silver plate instead of Nickel plate.

In [7], the grid antenna has a linearly polarized frequency scannable pencil beam and only one feed point per hundreds of radiating elements which make it especially suitable for HF, VHF and UHF frequencies when high gain antennas are needed. The current along the chain structure will acturally attenuate due to the radiation. Radiation from te parts parallel to the chain axis will add in phase in a certain direction. Radiations from the parts perpendicular to the chain axis will almost cancel each other due to opposite currents in each individual side of the loops.

A grid antenna is a radiation element of linear polization. As frequency changes, the beam direction varies due to the phase change in the current along the grid cells. In [8], a center fed grid antenna excited by coaxial line is presented. The antenna dimensions can be reduced by shorting the side length of each grid cell.

Convential printed circuits are designed and laid on printed circuit board (PCB) with solid ground plane. Multiple ground planes are also fabricated in a multilayered structure to minimize crosstalk between adjacent traces. However, metallic ground plane is easy to be stripped from substrate due to thermal expansion or humidity.

2 Feeding Method

The microstrip line feed are easy to fabricate and simple to match by controlling the inset position. However as the substrate thickness increases surface waves and spurious feed radition increase. Coaxial-line feed is also easy to fabricate and match, and it has low spurious radition. But it also has narrow bandwidth. Both method inherent asymmetries which generate higher order modes which produce cross-polarized radiation.

The aperture coupling feed are most difficult to fabricate and it also has narrow bandwidth, but easier to model and has moderate spurius radiation. The aperture coupling consists of two substrates separated by a ground plane. On the bottom side of the lower substrate there is a microstrip feed line whose energy is coupled to the patch through a slot on the ground plane separating the two substrate. A high dielectric material is used for the bottom substrate, and thick low dielectric constant material for the top substrate. The ground plane isolates the feed from the radiating element and minimizes interference of spurious radiation and polarization purity. The proximity coupling has the largest bandwidth (as high as 13 percent) and has low spurious radiation, but is somewhat more difficult to fabricate.

3 Lumped Element Model

To apply equivalent circuit analysis, first model segments in the meshes as equivalent lumped inductance and capacitance. Based on image theory, a conductor line with zero radius and with a distance a above ground plane can be viewed as two parallel conductors separated by $2a$ in free space, as shown in Fig 1. According to Ampere's Law, the magnetic flux per unit length, Ψ, and the vector potential $\bar{A}$

can be related as

$$\Psi = \iint_S \nabla \times \bar{A} \cdot \bar{s}$$

where $\bar{A}$ is related to the current distribution as

$$\bar{A}(\bar{r}) = \frac{\mu_0}{4\pi} \iint \frac{\bar{J}(\bar{r})}{|\bar{r} - \bar{r}'|} d\bar{r}'$$

where $\bar{J}$ is current density.

Assume that both conductors lie in the z direction, and carry current I and $-I$ respectively, then the vector potential has only z component, and can be written as

$$A_z(\bar{r}) = \frac{\mu_0 I}{2\pi} \ln \frac{r_1}{r_2}$$

where r_1 and r_2 are the distances from conductor 1 and 2, respectively, to the observation point.

A constant potential surface can be obtained by set $r_1/r_2 = p$. Thus, we have

$$\begin{cases} \ell = a(p^2+1)/(p^2-1) \\ R^2 - \ell^2 = -a^2 \end{cases}$$

Two cylindrical perfect conductors with radii R can occupy the region with centers at ($\pm\ell$, 0), respectively, without affecting the magnetic field distribution.

$$A_z = \frac{\mu_0 I}{2\pi} \ln \left(\frac{\ell + a}{R} \right)$$

The total magnetic flux, Ψ, between two conductors become

$$\Psi = \frac{\mu_0 I}{2\pi} \ln \left(\frac{\ell + a}{R} \right)$$

and the inductance per unit length L can be defined as

$$L = \frac{\Psi}{I} = \frac{\mu_0}{2\pi} \ln \left(\frac{\ell + a}{R} \right) = \frac{\mu_0}{2\pi} \ln \frac{R}{\ell - a} \tag{1}$$

Similarly, capacitance can be obtained by this procedure

$$C = \frac{\pi \epsilon_0}{\ln \frac{\ell + a}{R}} \tag{2}$$

4 Mesh Antenna

A meshed antenna, which metallic lines printed crossly on the substrate, is shown in Fig. 1(b). It can be divided into lumped elements as shown in Fig. 2(b), which shows the lumped circuit model at a junction of meshes. Applying KCL at the junction, we obtain the following equation

$$\begin{aligned} &\left\{ \omega C(dx + dy) - \frac{2}{\omega L dx} - \frac{2}{\omega L dy} \right\} V \\ &+ \frac{V_1 + V_3}{\omega L dy} + \frac{V_2 + V_4}{\omega L dx} = 0 \end{aligned} \tag{3}$$

Based on cavity model, the fundamental resonant frequency of patch antenna is given by $f_{010} = v_0/2L\sqrt{\epsilon_r}$, where L is the longest edge of the geometry and v_0 is the velocity of light in free space. Electric field of the resonance under the patch can be imaged as one-half cosecant curve which starts at one side of edge, zero at center, and becomes maximal negative at the opposite edge. However, the other direction of electric field is uniform.

The input impedance of patch and mesh varies with inset postion, because the impedance is proportional to the ratio of electric field to magnetic field. To match the coaxial and radiating element, we tune the coaxial position along the centerline of mesh. As the feeding position move to $L/2$, the input impedance tend to zero gradually, for the electric field vanishs at the center of mesh antenna at resonant frequency.

Due to that the feeding position does not affect the resonant frequency seriously, we use lumped element to model the mesh structure and predict the resonant frequency. Furthermore, the model also shows the current and voltage distribution, which gives the information to choose the feeding position in order to match the coaxial line.

5 Results and Conclusions

Near the coaxial feed point, the direction of current flow on the patch is omnidirectional, while that on the mesh antenna is limited on the metallic line, that is, the capacity of current of patch is large than mesh structure. So the input impedance of mesh is larger than patch. For the same characteric impedance coaxial feeding, in order to match radiating elements, the feed point of the mesh should be closer to center than that of patch.

The current distribution on the patch at the resonant frequency has only one direction. In the mesh case, we force the current to flow through metallic line, which has two direction crossing each other. The major current direction is the same as patch antenna, but there are some minor currents flowing orthogonally to the major current direction. These minor currents produce another polarization which is unwanted.

Fig 3(a) shows the comparison of the result obtained by simulation software HFSS and [9]. The FEM method used in HFSS shows good agreement results with FDTD method. The return loss of mesh antenna is shown ih Fig. 3(b). The width and length of outer dimension of mesh is 2 cm and 4 cm, respectively, and the width of the line, t, is 1 mm. The thickness of substrate is 0.75 mm and the dielectric constant is 4.4. The feed point is 1.4 mm away from the center point.

References

[1] H. Nakano, N. Suzuki, T. Ishii, and J. Yamauchi, "Mesh antennas for dual polarization," it IEEE trans. on Antennas and propagation, vol. 49, no. 5, pp. 715-723, May 2001.

[2] H. Nakano, T. Kawano and J. Yamauchi, "A cross-mesh array antenna," *11th International Conference on Antennas and propagation,* April 2001, IEE.

[3] G. Clasen and R. J. Langley, "Patch antennas constructed from meshes," *Antennas and Propagation Society, 1999. IEEE International Symposium 1999,* Vol. 4, pp. 11-16, July 1999.

[4] J. R. Jamesand G. Andrasic, "Superimposed dichroic microstrip antenna arrays," *Microwaves, Antennas and Propagation,* vol. 135, issue 5, pp. 403-312, Oct. 1988.

[5] L. T. Hildebrand and D. A. McNamara, "Experimental verification of an integral equation analysis of etched wire-grid antenna arrays," *Antennas and Propagation Society International Symposium AP-S. Digest 28,* pp. 1494-1497, June-2 July 1993.

[6] M. S. Wu and K. Ito, "Meshed microstrip antennas constructed on a transparent substrate," *IEICE trans.* vol. E74, No. 5, pp. 1277-1282, May 1981.

[7] M. Tiuri, S. Tallqvist and S. Urpo, "Chain antenna," *Antennas and Propagation Society International Symposium,* vol. 12, pp 274-277, Jun 1974.

[8] H. Nakano and T. Kawano, "Grid array antennas," *Antennas and Propagation Society International Symposium, IEEE*, vol. 1, pp. 236-239, July 1997.

[9] C. Wu, K. L. Wu, Z. Bi, and J. Litva, "Modelling of coaxial-fed microstrip patch antenna by finite difference time domain method," *Electronics Letters*, Vol. 27 Issue: 19, 12 Sept. 1991, pp. 1691-1692.

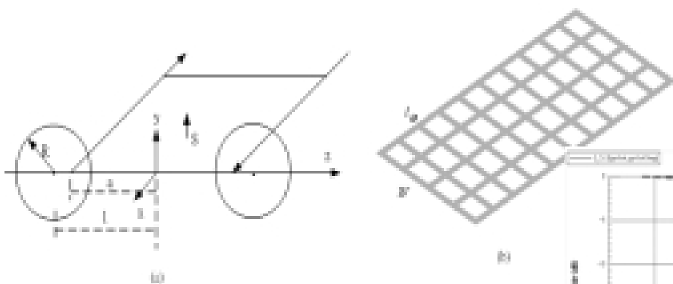

Figure 1: (a)Two circular conductor with separated by 2ℓ. S is a rectangle on the x-z plane with unit length along z axis.(b) Mesh antnna. L and W is the length and width of the mesh total dimension. The mesh antenna can be treated as combination of crossed microstrip line with t width.

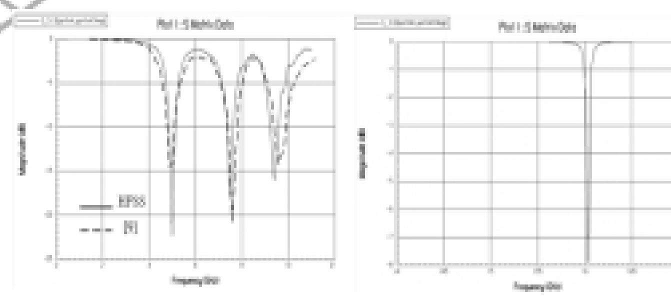

Figure 3: (a)The comparison of return loss of coaxial feed patch antenna and [9] (b)The comparison of return loss of mesh antenna and patch antenna.

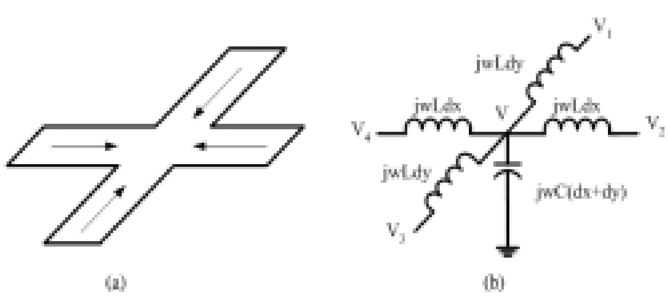

Figure 2: (a)The basic element of mesh antenna. (b)The microstrip line cross section modelled by lumped element.

Estimation of NLOS Effects with Scattering Models

Chun-Wei Wu and Jean-Fu Kiang
Department of Electrical Engineering and
Graduate Institute of Communication Engineering
National Taiwan University
Taipei, Taiwan, ROC

NSC 91-2213-E-002-030

Abstract

Estimation of mobile terminal location is made difficult by non-symmetric contamination of measured data caused by non-line-of-sight(NLOS) propagation effects. Three kinds of scatterer models are summarized to simulate the NLOS effect and compare to measurement result.

1 Introduction

Position location techniques is an important issue in recent years, a major thrust is the Enhanced 911(E911) phase II by the Federal Communications Commission(FCC), to be completed by October 2001. It requires that the wireless communication service providers must be able to report the location of all the E911 mobile stations with an accuracy of 100 m in 67% and 300 m in 95% in network-based methods, 50 m in 67% and 150 m in 95% in handset-based methods. Several propagation environment have been measured for analysing multipath characteristics in cellular networks. However, in a multipath propagation environment, very often the line-of-sight (LOS) paths are blocked, and only non-line-of-sight (NLOS) signals are available as data of range-based method. Estimate the performance of range-based method can be simiplified by replacing the practical measurement with the scatterer models.

2 Scatterer models

Parameters in the models will be verified by measuring statistics of TOAs of multipath signals [1]-[3]. While exact location of scatters depends on local surroundings, there are several models to approximately describe the topology of scatterers. These models are ring of scatterers(ROS), disk of scatterers(DOS) and Gaussian scatterer models. It is assumed that radiation patterns of the base station and mobile station antennas are omnidirectional in the horizontal plane.

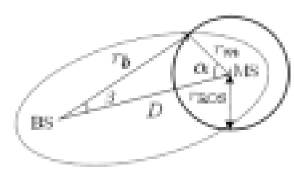

Figure 1: Ring of scatterers model.

2.1 Ring of Scatterers Model

In the ROS model shown in Fig.1, the scatters are assumed to locate on a ring of radius r_{ROS}, centered at the mobile station. The scatterers are uniformly distributed over $0 \leq \alpha < 2\pi$, with the probability density function(pdf) of

$$p^s_{\mathrm{ROS}}(r_{\mathrm{ROS}}, \alpha) = \begin{cases} 1/(2\pi r_{\mathrm{ROS}}) \\ \text{on the ring of scatterers} \\ 0, \\ \text{elsewhere} \end{cases}$$

The LOS distance between mobile station and base station is D, and the measured path length is μ. The associated NLOS delay is defined as $\eta = \mu - D$. The cumulative distribution function (cdf) in the ROS model is

$$F_{\mathrm{ROS}}(\mu \leq \mu_p) = 2\int_0^{\theta} p^s_{\mathrm{ROS}}(r_{ROS}, \alpha) r_{ROS} d\alpha$$

where μ_p is a given path length, $\theta = \cos^{-1}\left\{\left[r^2_{ROS} + D^2 - (\mu_p - r_{ROS})^2\right]/(2r_{ROS}D)\right\}$ is the marginal angle associated with μ_p, then the pdf associated with μ_i can be expressed as

$$p_{ROS}(\mu) = (\mu - r_{ROS})/\left\{r_{ROS}D \right.$$
$$\left.\sqrt{1 - \left[(D-\mu)(D+\mu-2r_{ROS})/(2r_{ROS}D) + 1\right]^2}\right\}$$
$$, D \leq \mu \leq D + 2r_{ROS} \qquad (1)$$

2.2 Disk of Scatterers Model

In the DOS model shown in the Fig.2, the scatterers are assumed to distribute uniformly within a circular disk with radius r_{DOS}. The pdf of scatterers can be expressed as

$$p^s_{\mathrm{DOS}}(r, \alpha) = \begin{cases} 1/(\pi r^2_{DOS}), & \text{inside disk} \\ 0, & \text{elsewhere} \end{cases}$$

As shown in the Fig.3, local coordinates de-

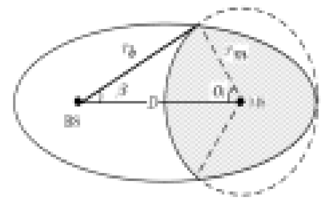

Figure 2: Disk of scatterers model.

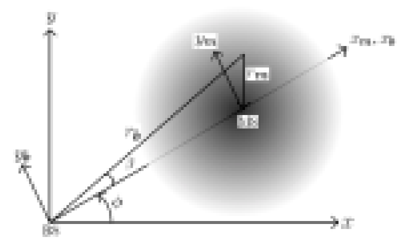

Figure 3: Local coordinates defined at BS and MS.

fined at the base station and mobile station are related by

$$\begin{aligned} x_b &= r_b\cos\beta = x\cos\phi + y\sin\phi \\ y_b &= r_b\sin\beta = -x\sin\phi + y\cos\phi \\ x_m &= r_m\cos\alpha = x_b - D \\ y_m &= r_m\sin\alpha = y_b \end{aligned}$$

where $r^2_m = r^2_b + D^2 - 2Dr_b\cos\beta$. The path length, μ, can be decomposed $\mu = r_b + r_m$, which is the sum of distances from the scatterer to mobile and base station, respectively. The time delay, τ, is related to the total path length as $c\tau = \mu$.

As shown in Fig.4, all points having a constant value of τ forms an ellipse with the base station and mobile station as its foci. To derive the pdf of TOA, first find the area between the interior of ellipse and the disk of scatterers.

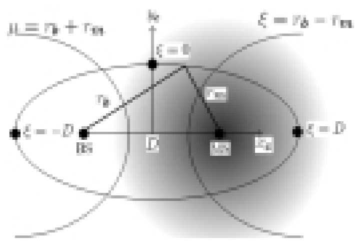

Figure 4: The ellipse(hyperbola) defined by the sum(difference) of r_b and r_m.

Take the derivation of the overlapping area divided by the total area of DOS gives the pdf of τ as

$$p_{\mathrm{DOS}}(\tau) = \frac{d}{d\tau}\frac{A_\tau(\tau)}{\pi r_{DOS}^2} \tag{2}$$

The area can be calculated using polar coordinate system defined at the mobile station, (r_m, α). Symmetry about the x axis can be used. Hence, the overlapping area can be expressed as

$$\begin{aligned} &A_\tau(\tau) = \\ &2\int_0^\theta \tfrac{1}{2} r_{DOS}^2 d\alpha + 2\int_\theta^\pi \tfrac{1}{2}\left(\tfrac{c^2\tau^2 - D^2}{2c\tau - 2D\cos\theta}\right)^2 d\alpha \\ &= r_{DOS}^2\theta + \int_\theta^\pi \left(\tfrac{c^2\tau^2 - D^2}{2c\tau - 2D\cos\theta}\right)^2 d\alpha \end{aligned} \tag{3}$$

To simplify (3), define $\tau_n = \tau/\tau_0$ and $D_n = D/r_{DOS}$, where τ_0 is the propagation time of line-of-sight between the base station and mobile stations. Thus, we have

$$\begin{aligned} &A_\tau(\tau) = r_{DOS}^2\theta + \tfrac{D^2(\tau_n^2-1)^2}{4}\left\{\tfrac{\tau_n\pi}{(\tau_n^2-1)\sqrt{\tau_n^2-1}}\right. \\ &+\tfrac{\sin\theta}{(\tau_n^2-1)(\cos\theta-\tau_n)} \\ &\left.+\tfrac{2\tau_n\tanh^{-1}\left[(1+\tau_n)\tan(0.5\theta)/\sqrt{1-\tau_n^2}\right]}{\sqrt{1-\tau_n^2}(\tau_n^2-1)}\right\} \end{aligned} \tag{4}$$

where $\theta = \cos^{-1}((D_n + 2\tau_n - D_n\tau_n^2)/2)$. Then, the pdf of TOA can be derived as

$$\begin{aligned} &p_{\mathrm{DOS}}(\tau) = \tfrac{r_{DOS}^2(D_n\tau_n-1)}{\sqrt{1-(D_n^2+2\tau_n-D_n\tau_n^2)/4}} + \\ &\tfrac{D^2}{4}\left\{\tfrac{\tau_n^2\pi}{\sqrt{\tau_n^2-1}} + \pi\sqrt{\tau_n^2-1}\right. \\ &+\tfrac{4\tau_n+D_n(2-6\tau_n^2)+D_n^2\tau_n(-1+\tau_n^2)}{2D_n\sqrt{1-(D_n^2+2\tau_n-D_n\tau_n^2)/4}} - \tfrac{2(2\tau_n^2-1)}{\sqrt{1-\tau_n^2}} \\ &\left.\tanh^{-1}\left[\tfrac{(1+\tau_n)\tan\left[\cos^{-1}(D_n/2+\tau_n-D_n\tau_n^2/2)\right]}{\sqrt{1-\tau_n^2}}\right]/2\right\} \end{aligned} \tag{5}$$

2.3 Gaussian Scatterers Model

Next, consider the Gaussian model when the scatterers are assumed to follow a Gaussian distribution. Define path difference, $\xi = r_b - r_m$, which form a hyperbola family orthogonal to the family defined by $\mu = r_b + r_m$. Thus, bipolar coordinates, (μ, ξ) are found. To determine the pdf of τ, $p(\tau)$, the scatterer density around the mobile is assume to follow a Gaussian distribution as

$$p_{\mathrm{G}}^s(x_m, y_m) = \frac{1}{2\pi\sigma_m^2}e^{-(x_m^2+_m^2)/2\sigma_m^2} \tag{6}$$

The pdf in bipolar coordinate system $p_G^s(\mu,\xi)$ can obtained by coordinates transformation as

$$p_{\mathrm{G}}^s(\mu,\xi) = \frac{\mu^2-\xi^2}{4\sqrt{\mu^2-D^2}\sqrt{D^2-\xi^2}}p_{\mathrm{G}}^s(x_m,y_m)$$

where

$$x_m(\mu,\xi) = \frac{\mu\xi}{2D} - \frac{D}{2}$$

$$y_m(\mu,\xi) = \frac{\sqrt{(\mu^2-D^2)(D^2-\xi^2)}}{2D}$$

The pdf of TOA is obtained form $p_{\mathrm{G}}^s(\mu,\xi)$ by integrating over all possible value of ξ at a fixed μ as

$$p_G(\tau) = 2c\int_{-D}^{D} p_{\mathrm{G}}^s(\mu,\xi)d\xi$$
$$= \frac{c\sqrt{\mu^2-D^2}}{2}\int_{-D}^{D}\frac{p_{\mathrm{G}}^s(x_m,y_m)}{\sqrt{D^2-\xi^2}}d\xi$$
$$+\frac{c}{2\sqrt{\mu^2-D^2}}\int_{-D}^{D}\sqrt{D^2-\xi^2}p_{\mathrm{G}}^s(x_m,y_m)d\xi \tag{7}$$

Substituting the Gaussian ditribution (6) into (7), we obtain

$$p_G(\tau) = \frac{c\sqrt{\mu^2-D^2}}{2}\int_{-D}^{D}\frac{1}{\sqrt{D^2-\xi^2}}\frac{1}{2\pi\sigma_m^2}e^{-r_m^2/2\sigma_m^2}d\xi$$
$$+\frac{c}{2\sqrt{\mu^2-D^2}}\int_{-D}^{D}\sqrt{D^2-\xi^2}\frac{1}{2\pi\sigma_m^2}e^{-r_m^2/2\sigma_m^2}d\xi \tag{8}$$

By defining $D_m = D/\sigma_m$, $D/c = \tau_0$, $\mu = c\tau_n\tau_0$, and $\xi = D\sin\theta$, (6) can be reduced to

$$p_G(\tau) = \frac{1}{4\pi\tau_0}\frac{D_m^2}{\sqrt{\tau_n^2-1}}$$
$$\int_{-\pi/2}^{\pi/2}(\tau_n^2-\sin^2\theta)\exp\left[-\frac{D_m^2(\tau_n-\sin\theta)^2}{8}\right]d\theta \tag{9}$$

2.4 Root Mean Squares

Root mean square(rms) delay spread can be defined as

$$\tau_{\mathrm{rms}} = \sqrt{\bar{\tau^2}-\bar{\tau}^2}$$

where $\bar{\tau^2}$ and $\bar{\tau}$ are the mean square and mean value defined as

$$\bar{\tau^2} = \int_D^{D+2r}\tau^2 p(\tau)d\tau, \qquad \bar{\tau} = \int_D^{D+2r}\tau p(\tau)d\tau \tag{10}$$

Here, $r = r_{ROS}$ in the ROS model, $r = r_{DOS}$ in the DOS model, and $r = \sigma_m$ in the Gaussian scatterers model. Notice that the defintions of mean square and mean value are different from those defined in measurements, where

$$\bar{\tau^2} = \sum_{k=1}^{K}\tau_k^2 P(\tau_k), \qquad \bar{\tau} = \sum_{k=1}^{K}\tau_k P(\tau_k) \tag{11}$$

where K is the number of time bins, $P(\tau_k)$ is the relative amplitude of multipath components fall in bin k. The measured rms delay spread is derived from a single power delay profile which is the temporal average of consecutive impulse response measurements collected and averaged over a local area. Assume that the scatterers around the mobile and base stations have similar scattering characteristics, then the signal strength in each time bins is roughly proportional to the number of scatterers that contribute to that time bin. Here, (10) can be assumed to be equivalent to (11).

3 Simulations

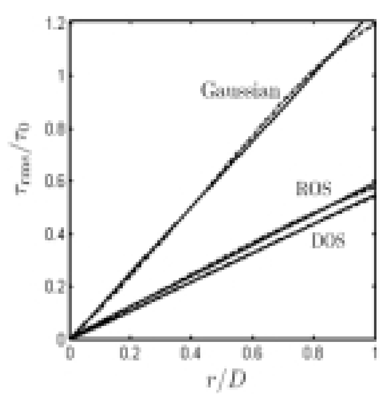

Figure 5: Normalized rms delay spread as a function of size parameter in scatterer models, ——:regression line, - - -:scatterer model.

The rms delay spread can be related to the parameters of scatterer model. Regression analysis is also applied to the results of ROS, DOS and Gaussian scatterer models, respectively, as shown in Fig.5. Radius of scatterer models can be related to τ_{rms} as

$$r_{ROS} = 1.67c\tau_{\mathrm{rms}}$$

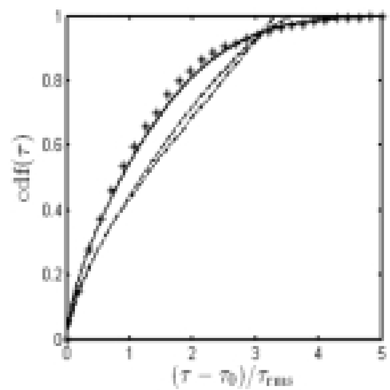

Figure 6: Distribution of TOA for ROS, DOS and Gaussian model, ——: Gaussian model, - - -: DOS model, -·-·-: ROS model, * : measurement[4].

$$r_{DOS} = 1.82 c \tau_{\rm rms}$$
$$\sigma_m = 0.79 c \tau_{\rm rms} \tag{12}$$

Fig.6 shows the comparison of cumulative distribution function of delay for DOS and Gaussian model. The measured data in [4] are also marked for comparison. The measured rms delay spread is 0.682 μs, and LOS distance is 1,500 meters. The Gaussian model matches better with the measurement than the DOS model.

References

[1] S. Al-Jazzar, J. Caffery, Jr. and H. R. You,"A scattering model based approach to NLOS mitigation in TOA location systems," *IEEE Veh. Technol. Conf.*, vol.2, pp.861-865, 2002

[2] R. B Ertel and J. H. Reed,"Angle and time of arrival statistics for circular and elliptical scattering models," *IEEE J. Selected Areas in Commun.*, vol.17, no.11, pp.1829-1840, Nov 1999

[3] R. Janaswamy, "Angle and time of arrival statistics for the Gaussian scatter density model,"*IEEE Tran. Wireless Commun.*, vol.1, no.3, pp.488-497, Jul 2002

[4] K.I. Pedersen, P.E. Mogensen and B.H. Fleury, "A stochastic model of the temporal and azimuthal dispersion seen at the base station in outdoor propagation environments," *IEEE Trans. Veh. Technol.*, vol.49, no.2, pp.437-447, Mar. 2000